Fusion Engineering and Design 206 (2024) 114608

Contents lists available at ScienceDirect

Fusion Engineering and Design

journal homepage: www.elsevier.com/locate/fusengdes

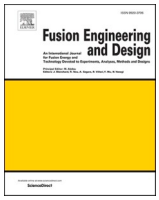

Thermomechanical analysis of tungsten-copper joints for fusion applications using digital image correlation

Younes Belrhiti [a,*], Cory Hamelin [b], David Knowles [a,c], Mahmoud Mostafavi [a]

[a] Department of Mechanical Engineering, University of Bristol, Bristol BS8 1TR, UK
[b] Culham Science Centre, UK Atomic Energy Authority, Abingdon, Oxfordshire OX14 3DB, UK
[c] Henry Royce Institute, Manchester M12 9PL, UK

ARTICLE INFO

Keywords:
Fusion
Plasma facing components
DEMO
Digital image correlation
Creep-fatigue

ABSTRACT

The European DEMOnstration Fusion Power Plant DEMO represents a significant milestone in the progression towards sustainable fusion energy and a critical phase between ITER and commercial fusion reactors, aiming to demonstrate sustained net positive electricity production. Thanks to its properties, tungsten is a promising material for divertor armor. Coupled with copper alloys as heatsinks, they offer robust thermal management properties to deal with intense thermomechanical loads and irradiation damage. Understanding the thermomechanical behaviour of tungsten-copper joints during their application is then necessary for divertor design.

This study presents experimental analysis on tungsten-copper brazed materials subjected to thermomechanical solicitations to simulate mono-block conditions with heat fluxes expected to reach 20 MW/m^2 and so to face potential creep-fatigue failure. The experimental tests were coupled with Digital Image Correlation up to 400 °C to analyse the thermomechanical behaviour of these joints, providing insights into their thermal behaviour, structural integrity, damage accumulation, joint failure and identification of strains required for creep-fatigue assessment using design codes.

1. Introduction

Currently, attention is turning to the European DEMOnstration Fusion Power Plant (DEMO) [1–4] which is expected to be capable of demonstrating the production of net positive sustained electricity representing the step between ITER and a commercial reactor. DEMO design dictates that in-vessel components face significant thermomechanical loads, and severe damage due to high thermal load cycles, coupled with high electromagnetic loading and unprecedented levels of irradiation damage.

The divertor is an in-vessel component with multiple essential functions, including particle exhaust, heat removal, and plasma confinement. The divertor comprises a bonded structure of an armor segment on the plasma side and a heatsink segment on the cooling tube side. Thanks to its properties, tungsten (*W*) is one of the most promising candidates for the armor material of divertors [3,5,6]. *W* has the highest melting point among elementary metals (3400 °C), it is resistant to plasma erosion owing to the high bonding energies of atoms for its large atomic number, and it is largely compatible with hydrogen present (in the form of tritium) within conventional tokamak designs. High heat influx from high-temperature plasma in a fusion reactor is received by the *W* armor of the divertor. The thermal energy is then transferred to the coolant, currently planned to be water, through the heat sink [7,8]. Copper (*Cu*) alloys are the candidate materials for the heat sink of a water-cooled target thanks to their thermal properties such as high conductivity and also easy formability [1,9].

In developing the DEMO divertor, the design of joints between tungsten to other fusion-related materials is a significant challenge as a result of the dissimilar physical metallurgy of the materials to be joined [10,11]. For the bond between the armor and heatsink segments, various techniques have been investigated, such as brazing [10,12,13], electron beam welding [14,15], explosive welding [16,17], and friction stir welding [18,19]. At present, brazing *W* to *Cu* at temperatures around 1000 °C in a vacuum environment [14,15] is the preferred process in terms of thermal conductance. However, analyses for the duplex structure reported that large shear stress appears at the interface [20].

Since heat fluxes up to 20 MW/m^2 are expected on the divertor plate in DEMO, creep at elevated temperatures accelerates the damage due to thermal fatigue and becomes a critical failure mode if the operating temperature is above the negligible creep temperature for the material.

* Corresponding author.
E-mail address: younes.belrhiti@gmail.com (Y. Belrhiti).

https://doi.org/10.1016/j.fusengdes.2024.114608
Received 3 June 2024; Received in revised form 18 July 2024; Accepted 22 July 2024
Available online 31 July 2024

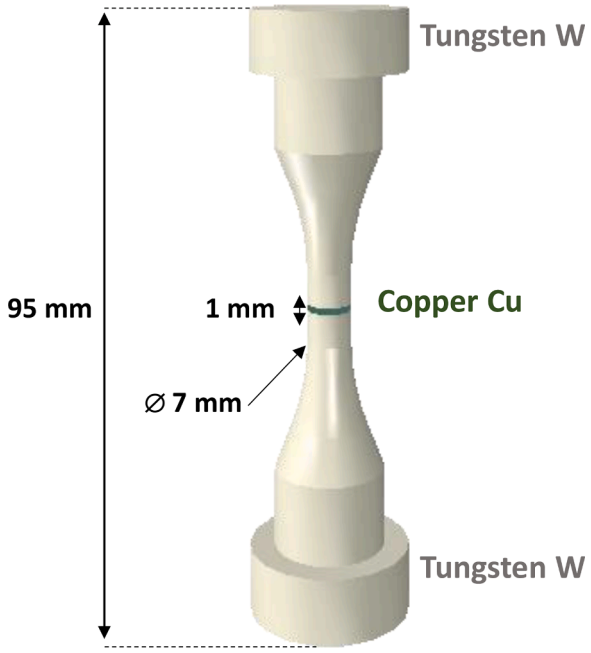

Fig. 1. W/Cu sample geometry.

In the monoblock, it is expected that the interlayer (*Cu*) exceeds 350 °C and is below 500 °C [21]. Considering the plasma-facing tungsten armour's functionality is dependent on its temperature being controlled by its integral attachment to the heat sink, the structural integrity of tungsten-copper joints is critical. It has been shown previously that for operation conditions fatigue damage of *W* armour due to thermal stress does is not consequential and that the service life of the divertor is determined by its thermal fatigue of either the braze interface region or the copper substrate heat sink [20]. Therefore, a better knowledge of the thermomechanical behaviour of the braze interface and the substrate *Cu* is essential to designing divertor plates with *W* brazed to *Cu*.

Digital Image Correlation (DIC) [22–34] is based on the analysis of successive digital images of the same sample during a mechanical test. The DIC process consists of calculating displacements on specific points of several subsets which constitute a grid between the image corresponding to an unloaded state and the deformed image recorded during the test. From these displacements, strains are calculated. DIC is used for various purposes such as the evaluation of local changes in a wide range of materials due to their heterogeneity, the description of the cracking process and the validation of theoretical and numerical models.

This paper presents experimental results on the thermomechanical behaviour analysis realised on tungsten-copper samples (*W/Cu),* which are manufactured by vacuum brazing, using a uniaxial test with a thin layer of *Cu* sandwiched between *W* subjected to compressive load to mimic the mono-block conditions with the aim to better understand and generate new knowledge to predict their performance in terms of structural integrity, damage accumulation, joint failure and identification of the required strain values for creep-fatigue service life assessment using design codes [35]. For this reason, tests were coupled with DIC at high temperatures.

2. Experimental

2.1. Material

6 samples were manufactured by vacuum brazing at 1020 °C, whereby two pieces of tungsten were joined to a copper disc 1 mm thick [36] using gold foil as a filler material.

W/Cu samples were prepared to include the interlayer of copper (99.95% Cu), 1 mm thick, at the centre of the specimen sandwiched between tungsten (99.9%) ends (Fig. 1).

2.2. Thermomechanical and optical testing

The experimental setup (Fig. 2a) includes an electromechanical Zwick-Roell Kappa 100 testing machine. The axial strain is measured using two capacitive extensometers shown in Fig. 2b, with a 13 mm spacing between them. The tests are conducted at 400 °C to be sufficient to cause creep while avoiding potentially damaging oxidization [36]. A LAVISION Digital Image Correlation kit was used to perform optical measurements. It includes two M-lite 5 M 12-bit CMOS USB3 cameras (2448 pixels × 2048 pixels) coupled with Tokina macro 100 f2.8D lenses. Two cameras were used for the non-planar geometry of the sample, enhancing accuracy and resolution compared to a single-camera 2D setup. For high-temperature measurements, a blue light source was used so that the two cameras could capture high-quality images through the observation window of the furnace [37] as shown in Fig. 2a. A pinhole calibration plate (11×11 marks) was used in direct contact with

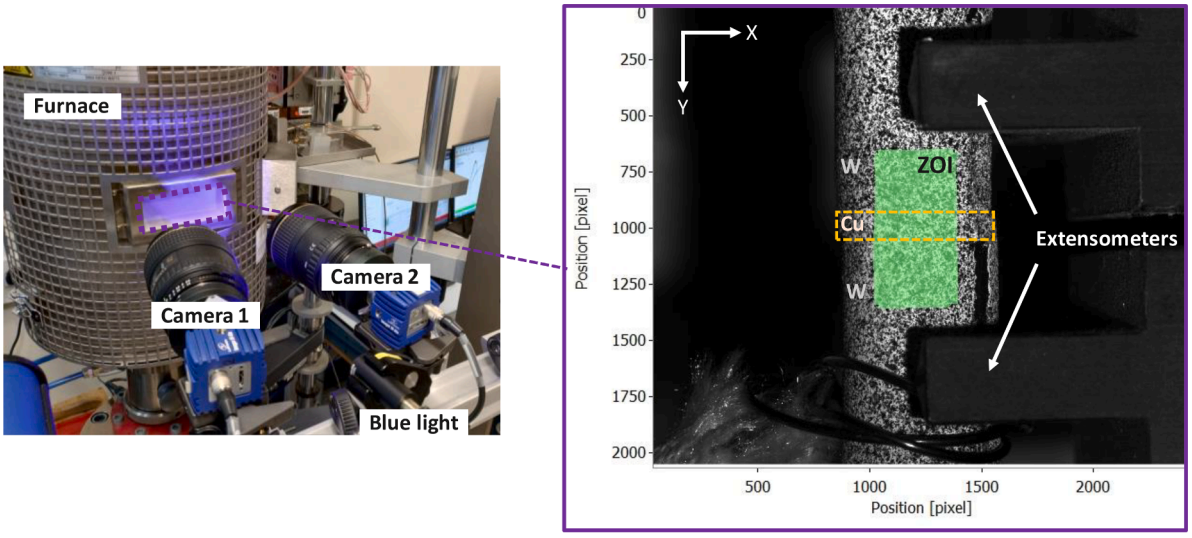

-a- -b-

Fig. 2. Experimental setup (-a-) and example of recorded images of W/Cu using DIC (-b-).

Table 1
DIC parameters.

	DIC parameter	Value	
Calibration parameters	Focal length *f*	132.15 mm	
	Pixel size	0.00345 mm	
	Scale factor	100.19 pixel/mm	
	Camera position relative to calibration plate	**Camera 1** Translation (1.75, −9.02, 385.40) mm Rotation (−1.34, −16.40, −178.79) °	**Camera 2** Translation (−8.32, −6.55, 395.38) mm Rotation (−0.69, −2.72,179.24) °
Analysis parameters	Subset size	45 pixels	
	Step size	15 pixels	
	Subset shape function	Affine transformation with 6 degrees of freedom	
	Correlation mode	Relative to first	
	Strain formulation	Right Cauchy	

the sample at room temperature, using the same cameras. The furnace window remained fixed after calibration. The extensometers and thermocouples were added through the back side of the furnace. The DIC calibration and analysis parameters are given in Table 1 [38].

The zone of interest (ZOI) for DIC, on which strains calculation is done, is represented in Fig. 2b. Each pixel of these images stores a grey level value due to a pattern at the surface. To avoid ambiguities in the matching process, a speckle pattern is used to highlight the contrast. A white opaque paint layer is deposited on the surface of the sample using an aerosol spray and then dried. After that, black drops will be carefully projected using spray paint. Droplets are randomly spread and their size is variable (contain around 3 – 15 pixels per droplet). DIC software used here is StrainMaster [39] and the system was calibrated using calibration plates at room temperature.

Four test conditions were considered:

- The first test was performed to analyse the thermal behaviour due simply to internal stresses generated by thermal expansion mismatch while heating, i.e., no external load was applied. Images were captured at regular intervals during heating up to 400 °C, with a heating rate of 5 °C/min.
- The second test was carried out to assess thermomechanical behaviour under cyclic loading without significant creep (zero dwell). The cyclic load was from 0 N to −5000 N (−120 MPa) to represent expected operating conditions for the mono-block [36]. The test was conducted under load control with a ramp rate was 2500 N/min.
- The third test aimed to investigate two creep-fatigue conditions achieved by varying the dwell time (20 s and 200 s) at constant peak compressive load (−5000 N/−120 MPa) to increase the creep component of the creep-fatigue process under load control with a ramp rate of 2500 N/min.
- The fourth test aims to identify the failure region of *W/Cu* achieved by conducting strain-controlled tests after the sample's thermal soak with a dwell time of 200 s.

For the second, the third and the fourth tests, the test temperature was 400 °C. The frequency of image acquisition was 1 image/s.

In this paper, the first, the second and the third tests were conducted on the same sample. The fourth test was conducted on the second sample. The results were confirmed using the other samples.

The applied load value was selected according to a previous study in which a *W/Cu* specimen (represented in Fig. 1) was modelled [36]. It was identified that the best matching between the *W/Cu* specimen model (Fig. 1) and the *Cu* interlayer of the mono-block (an average cyclic strain of −0.78% in the considered section) was obtained in *Cu* section of the specimen when applying a compressive displacement of 3.0e-5 m. It was noted that the reaction force at the displacement of *W/Cu* model converges toward ~ −5000 N [36].

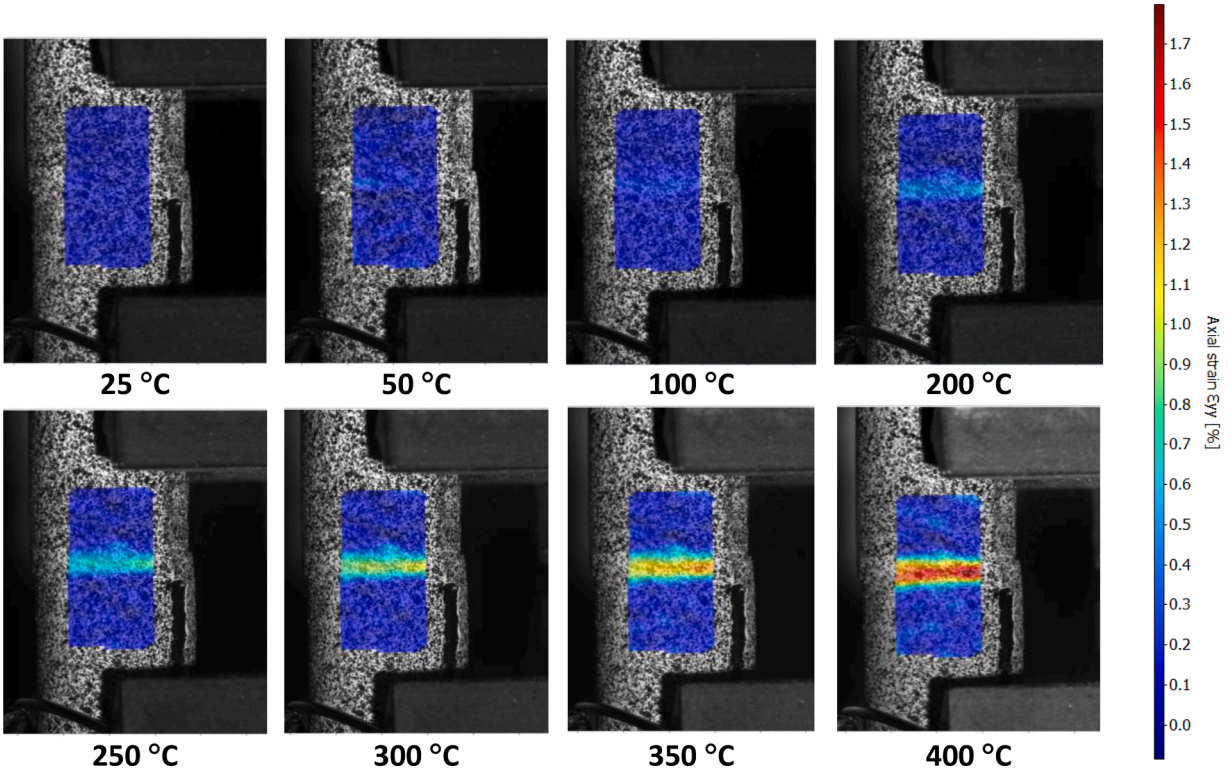

Fig. 3. DIC strain maps obtained during heating.

Table 2
Thermal properties of the considered materials at different temperatures (from Ref. [9]).

Material	Temperature (°C)	Thermal expansion coefficient (10^{-6} K^{-1})
W	20	4.5
	500	4.7
OHFC—Cu	20	16.7
	200	17.2
	400	17.8

3. Results

3.1. Thermal behaviour of W/Cu

Ten reference images at room temperature were recorded, and then images were recorded at regular intervals while heating up to 400 °C.

Fig. 3 represents the evolution of DIC axial strain maps generated. At around 200 °C, normalised thermal expansion arises in the middle of the ZOI represented in Fig. 2b corresponding to the *Cu* braze.

The normalised thermal expansion increases with temperature until reaching a value of around 1.7% on the *Cu* surface and around 0.7% in the *W* interface at 400 °C.

This is justified by the thermal expansion mismatch between *Cu* and *W*.

Literature values of the thermal expansion coefficient of these materials at specific temperatures are given in Table 2.

3.2. Mechanical characterization

3.2.1. Structural integrity

The second test is realized to check the sample behaviour under pure compressive fatigue (zero second dwell). At elevated temperatures, even under minimal applied stress, pure *Cu* can experience considerable creep deformation. For instance, at 400 °C and 100 MPa, the creep rate of pure *Cu* can reach as high as 10^{-4} s^{-1} at 100 MPa at 400 °C [40]. The cyclic load is from 0 N to −5000 N to achieve the match with mono-block conditions [36] at 400 °C. The three cycles were conducted and represented in Fig. 4. This test was conducted after the stabilization of the temperature at 400 °C as in real conditions, the divertor faces 400 °C

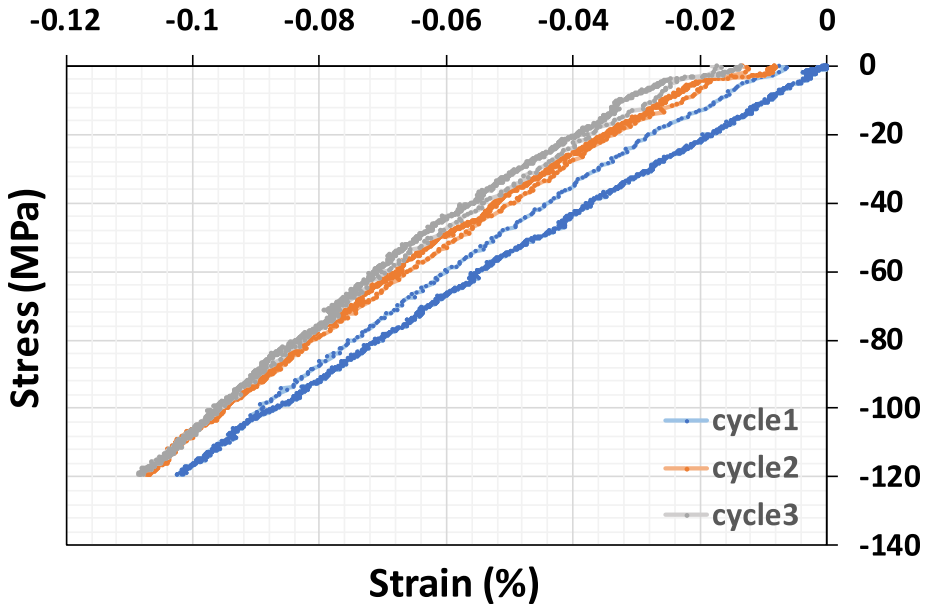

Fig. 4. Compressive behaviour of W/Cu duplex structure.

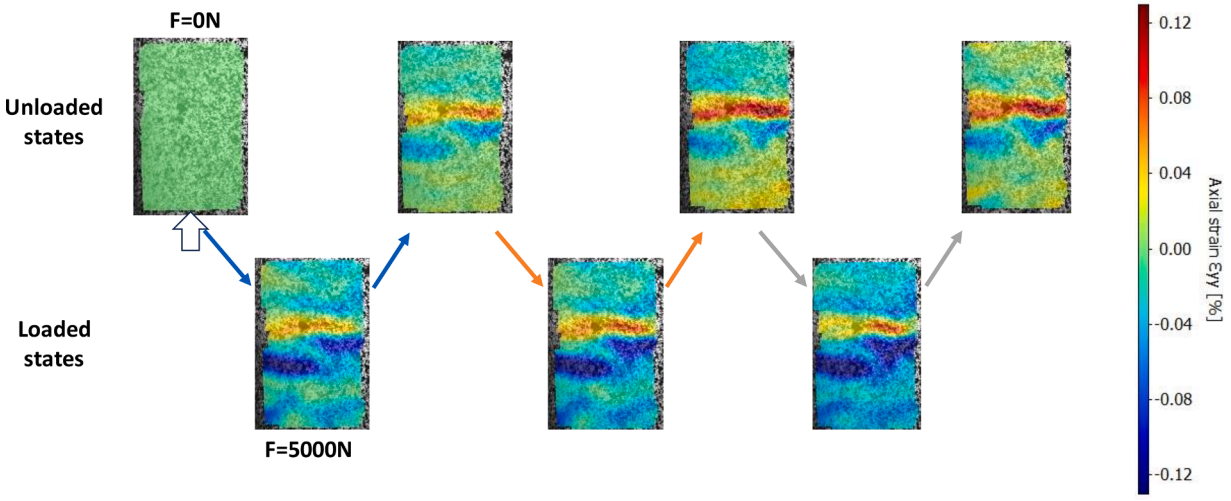

Fig. 5. DIC ε_{yy} strain maps for the three cycles in unloaded and compressive loaded states.

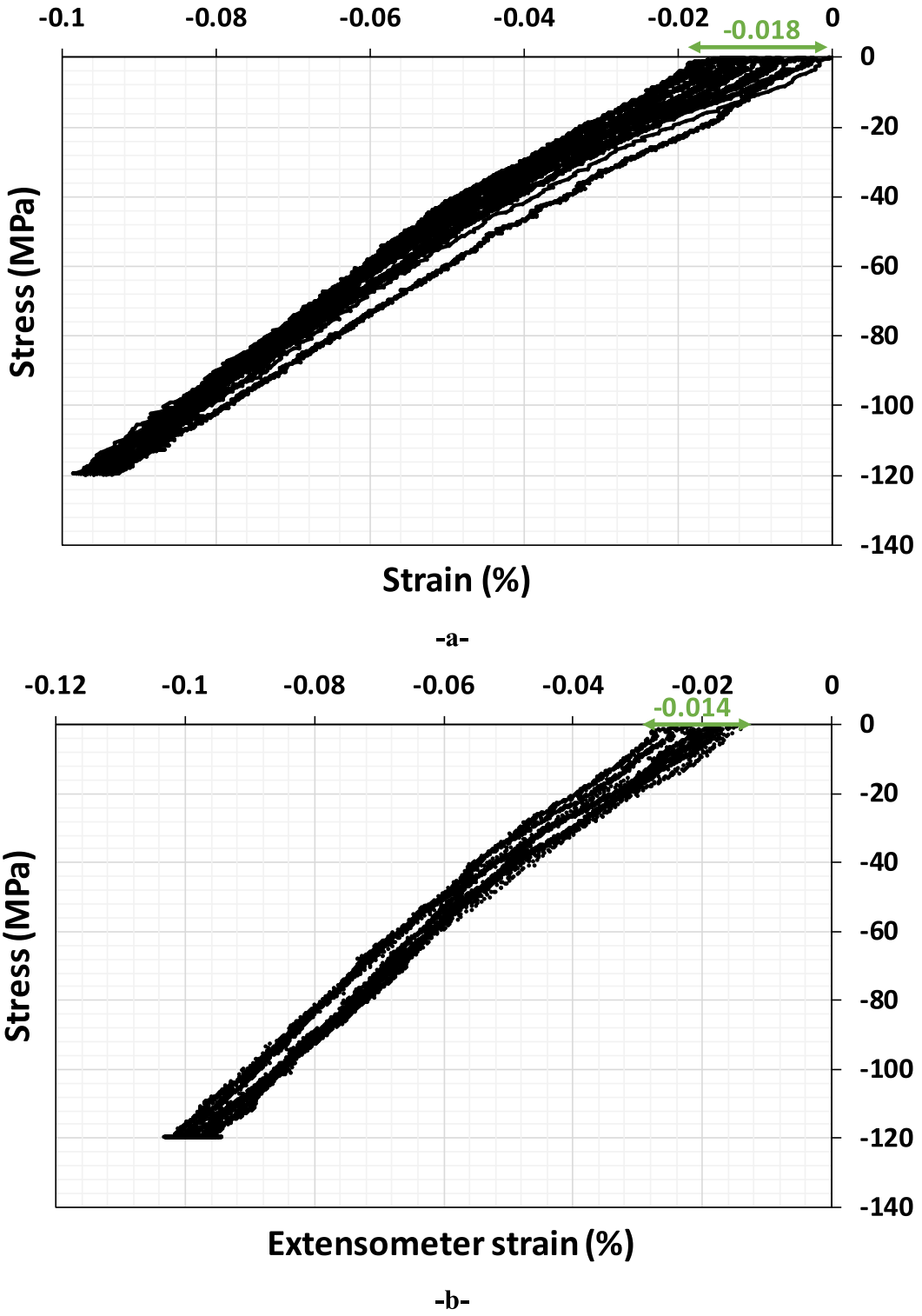

Fig. 6. Compressive stress-strain curves for 10 successive cycles with a dwell time of 20 s (-a-) and 200 s (-b-).

temperature for less than 2 h.

Thanks to DIC, strain maps were represented for each cycle at the unloaded state and the loaded one corresponding to the maximum applied compressive load. To do so, 10 reference images were recorded before starting the test.

This test confirms the absence of sample buckling and deformation due to the compressive load in addition to the absence of any shift between the brazed parts due to the presence of shear stresses [20].

The strain distribution due to the compressive stresses of the test calculated by DIC is represented in Fig. 5.

In the unloaded states of the 3 cycles, in the *Cu* surface and *W/Cu* interface, tensile strains due thermal expansion of *Cu* are present as shown in Fig. 3 and explained above.

In the loaded states, compressive strains appear in the lower *W* part, which is in direct contact with the movable crosshead. Tensile strains in the *Cu* surface and *W/Cu* are still present but with low intensity in comparison with the unloaded state. The compressive strains on the upper part of the sample *W* are low in comparison to the lower *W* part.

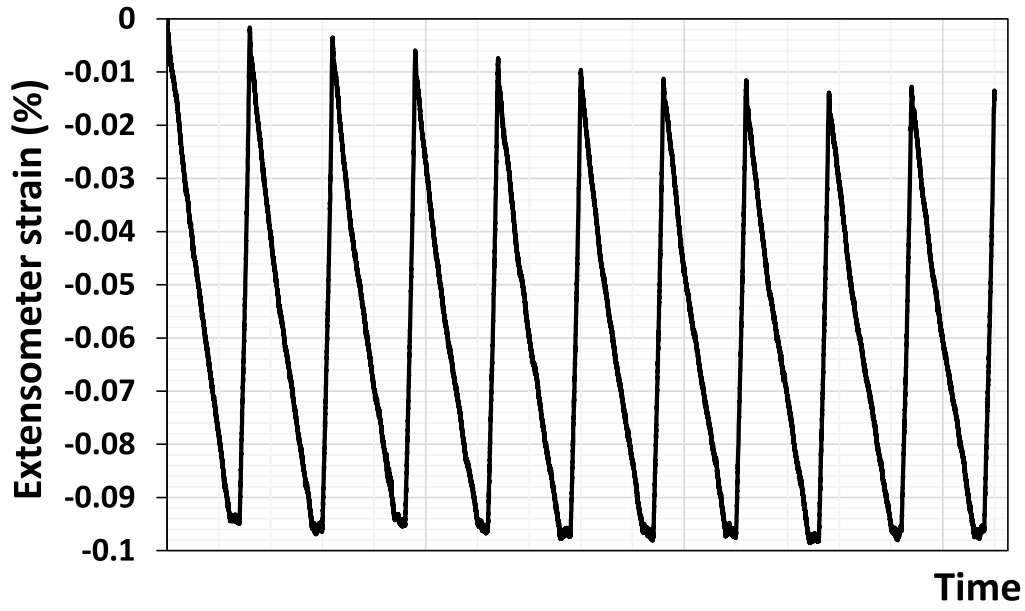

-a-

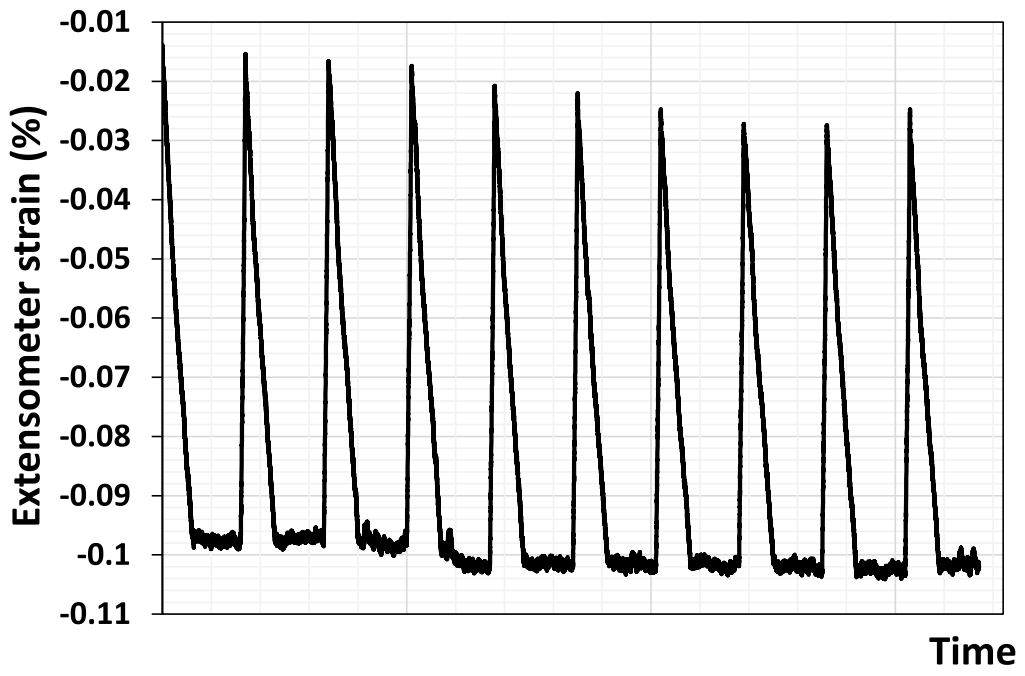

-b-

Fig. 7. Strain evolution versus time for 10 successive cycles with a dwell time of 20 s (-a-) and 200 s (-b-).

This observed difference in strain values can be attributed to misalignment between the brazed parts and the presence of defects, in addition to strain accumulation within the copper layer.

The intensity of compressive strains noticed increases as the test progresses. For the same applied load (−5000 N), the compressive strains are higher in cycle 3 in comparison with cycle 1 which confirms the accumulation of the compressive strains.

3.2.2. *Creep-fatigue deformation*

To underline the impact of dwell time on the compressive damage accumulation, the following test is done to include a dwell time at the maximum applied stress and so investigating two creep-fatigue conditions (a dwell time of 20 s then 200 s). 10 cycles are applied for each condition on the same specimen, i.e., 10 cycles with a 20 s dwell are followed by 10 cycles with a 200 s dwell.

Fig. 6a and Fig. 6b correspond respectively to the bulk compressive stress-strain curves with a dwell time of 20 s and 200 s.

Fig. 7a and Fig. 7b correspond respectively to the evolution of strain versus time in the successive 10 compressive cycles of each dwell condition to underline the cyclic strain drop.

The strain values obtained thanks to DIC (Fig. 5) and the extensometers (Fig. 6) indeed differ because they measure different types of strain. Fig. 5 represents local measurements within subsets of 45 pixels (Table 1). The extensometer measures strains on the *W/Cu/W* layers, as

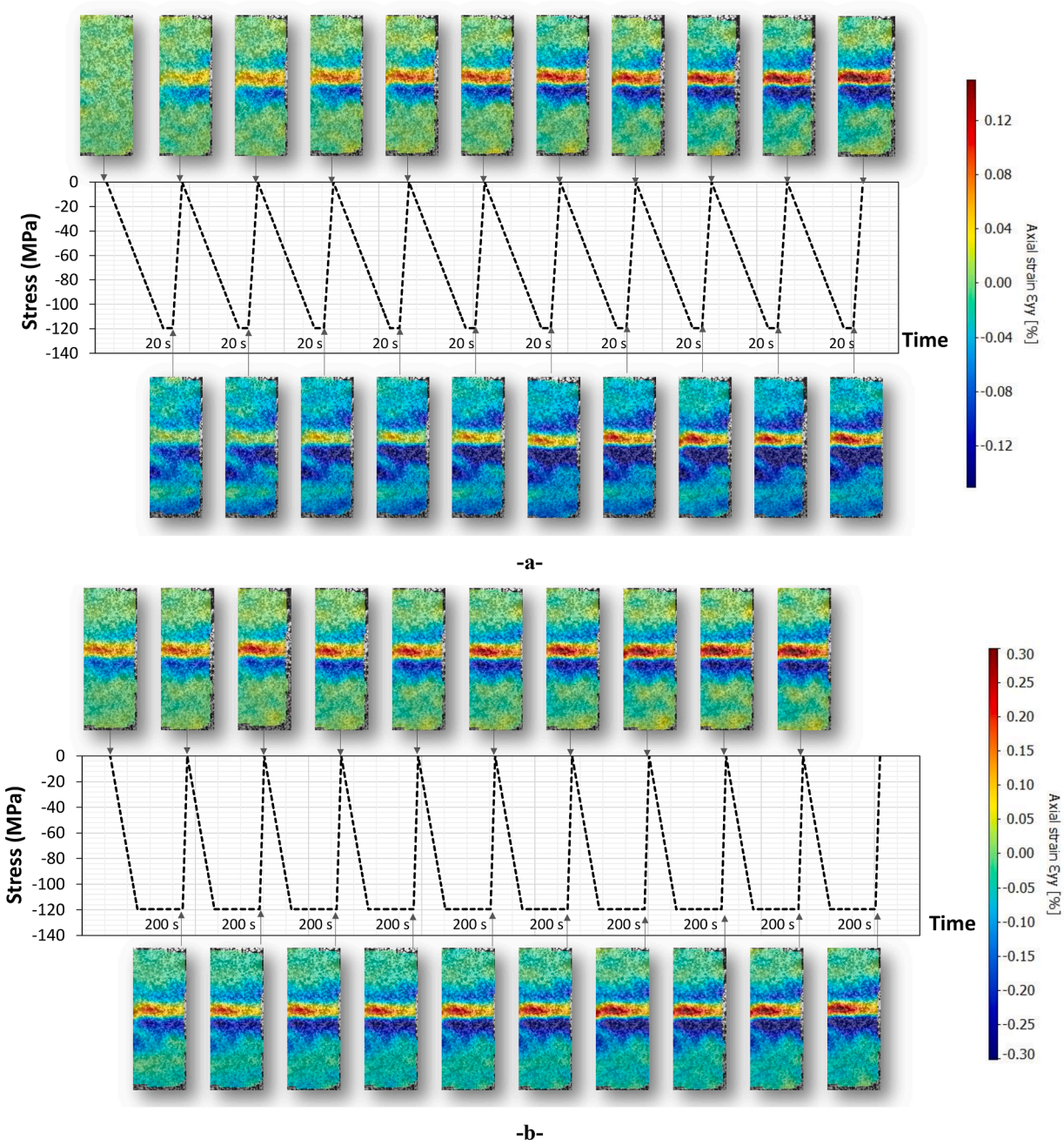

Fig. 8. Axial strains ε_{yy} obtained in the creep-fatigue tests with 20 s (-a-) and 200 s (-b-) dwell time.

illustrated in Fig. 2, with a 13 mm spacing between them.

Regarding the extensometer readings for the 200 s dwell experiments, we acknowledge the importance of zeroing before use. In this specific instance, the decision not to zero the extensometer between tests was deliberate. The tests were conducted consecutively to highlight the impact of strain accumulation within the copper layer. This approach was intended to demonstrate how strains evolve over successive tests with different dwell time.

The compressive loading did not induce any buckling or any shift between the brazed surfaces due to the presence of shear stresses. The compressive strains cumulated after 10 cycles are around −0.018% for the condition with 20 s dwell time (Figs. 6a and 7a) and −0.014% for subsequent cycles with 200 s dwell time (Figs. 6b and 7b).

Fig. 8a and b represent the axial strain maps obtained by DIC at different states (loaded and unloaded) during the 10 cycles for the two conditions.

The strain distribution is quite similar to the strain distribution of the pure fatigue test presented before.

The presence of tensile strains on the *Cu* surface and the *W/Cu* interface was generated due to the thermal expansion of *Cu*. These strains are higher in the unloaded states and decrease slightly in the loaded state in the case of 20 s dwell. For the condition with a longer dwell time (200 s), the strains are like the unloaded state in the last cycles.

Compressive strains are high in the lower *W* part of the sample, which is in contact with the movable crosshead, in comparison with the higher part of *W*. These strains remain present throughout the test, even in the unloaded states. Some of these differences can be due to the manufacturing process and misalignment. The parent metal experiences insignificant change, such that the observed bulk response is localised predominantly at the *W/Cu* interface.

To better understand the behaviour of *Cu* and *W* and the strain

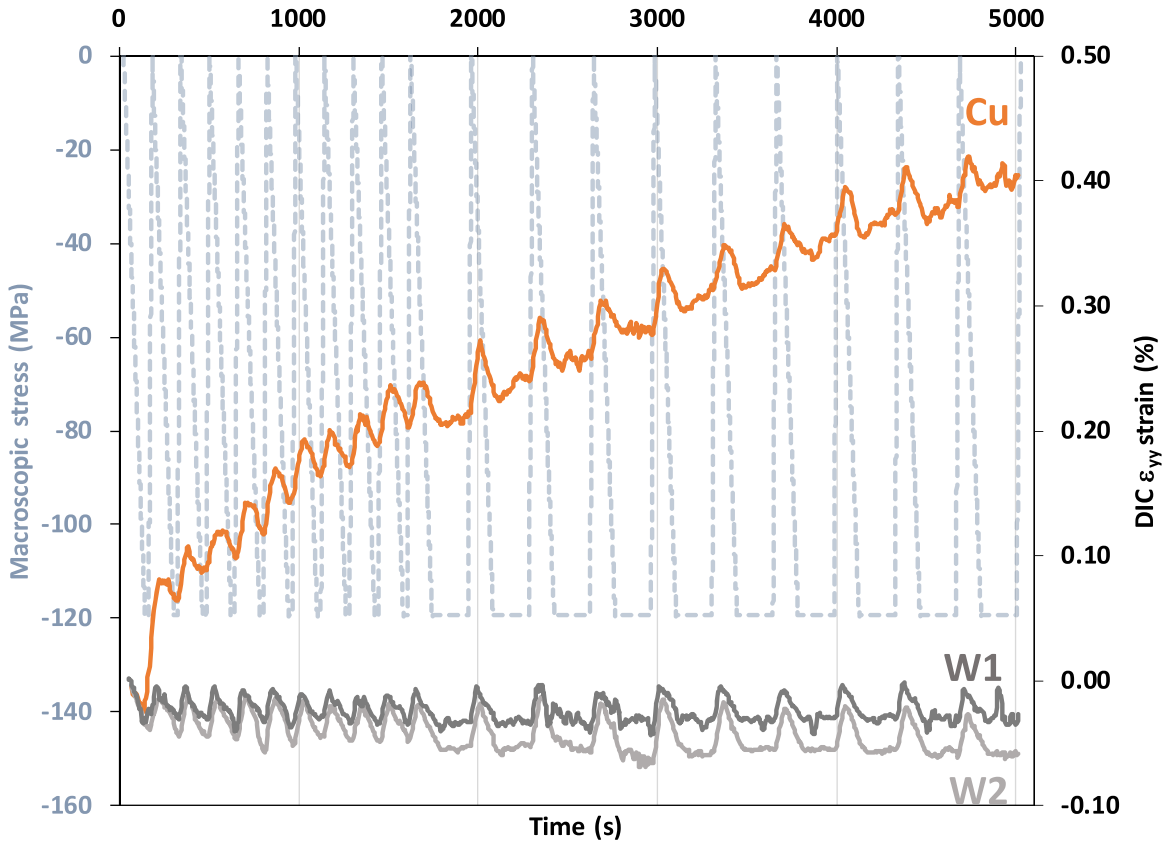

-a-

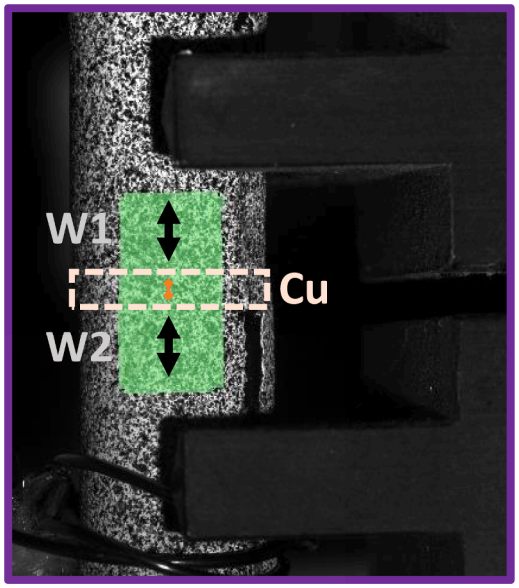

-b-

Fig. 9. Local axial strains ε_{yy} obtained using DIC during the creep-fatigue test (-a-) at specific positions on the surface of Cu and W represented in (-b-).

distribution under creep-fatigue test, the axial strain ε_{yy}, obtained using DIC, corresponding to the *Cu* surface and the upper and lower part of *W1* and *W2*, was calculated separately using the exported displacements from StrainMaster at a specific location. Fig. 9a represents the evolution of strain versus time during the creep-fatigue test: 10 cycles with 20 s dwell time followed by 10 cycles with 200 s dwell time.

After reaching 400 °C, the DIC strain values calculated on *Cu* tend to increase over time when subjected to a creep-fatigue test at this temperature which is the result of creep in tension. This evolution is mitigated cyclically by the increase of the applied compressive load. Upon unloading, strain evolution highly increases which corresponds to the elastic recovery. This data suggests creep in *Cu* is significant during

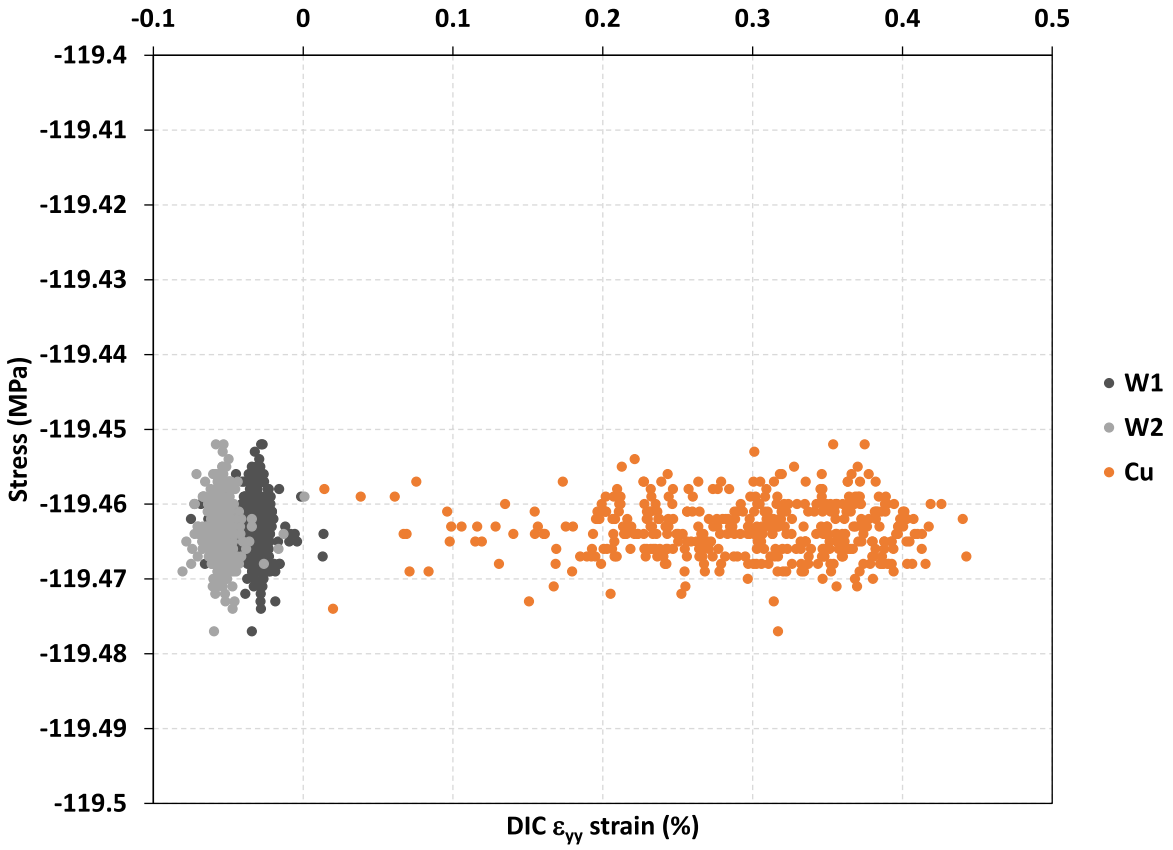

Fig. 10. The accumulated DIC ε_{yy} strain during the successive cycles during at the dwell time.

longer dwells, suggesting this will be the life-limiting mechanism and not thermal fatigue.

In Fig. 8, compressive strains are evident in both sections of *W*. Fig. 9 confirms this highlighting that the local compressive strains in the lowest part (*W2* in Fig. 9b), which directly interfaces with the movable crosshead, exceeds those locally measured in the upper part, *W1* (Fig. 9b). This can be justified by the attenuation of compressive impact within *W1* due to the expansion of *Cu* and the misalignment related to the manufacturing process. For *W1* and *W2*, the strain evolution is directly impacted by the applied compressive load. During unloading, elastic recovery is noticed for each cycle. The expansion of *Cu* does not impact the global compressive behaviour of the sample due to the thickness of *Cu* in comparison to *W*.

Strains cumulated at the maximum applied compressive load corresponding to the dwell time 20 s and 200 s of the different cycles are represented in Fig. 10. These values confirm the rigidity of *W*.

3.2.3. *Mechanical fracture*

To identify the failure zone of *W/Cu*, strain-monitored tests were performed after reaching the sample's thermal soak. A strain-monitored creep-fatigue test (±0.4%) was conducted with a dwell time of 200 s. Dwells were applied at both peak (global) tension and peak (global) compression. The test was coupled with DIC and the ZOI was adapted to focus on the center of the sample. Fig. 11a represents the axial strain maps calculated at the end of each dwell time in tension and compression. Fig. 11b represents the strain maps in tension with an adequate scale to underline the initiation of tensile strain in voids.

Fig. 11a underlines the initiation of strain concentration in the interface between *W* and *C* (yellow colour) and after reaching a specific cycle number, a concentration of tensile strains appears in particular locations corresponding to voids (red colour). These strains correspond to the creep damage initiation and their intensity increases as the test progresses. At the 5th cycle, tensile strains initiated in the void on the left side of the interface in the ZOI remain present under compression, indicative of persistent material failure.

Additional tests were conducted to underline the intensification of creep damage in the interface (±0.6%, ±0.8% and ±1%).

Fig. 12 represents the evolution and growth of creep damage in the interface through the creep-fatigue cycles at the condition ±1%. Each strain map was calculated at the end of each tensile creep dwell. The creep damage strain increases through the tests, intensifying along the same trajectory through the interface. The nonlinearity of the trajectory is due to the geometry of the interface between *W* and *Cu*, which is not flat.

The evolution of strain distribution in tension and compression is represented in video1 (Supplementary material) and the intensification of strains related to creep damage within the same cycle (10th cycle) during the dwell time in tension is clearly shown in video2 (Supplementary material).

DIC confirms the presence and the intensification of creep damage, generally assumed to be an intergranular mechanism associated with the nucleation, cavitation, and coalescence of cavities and voids which makes creep damage a distributed mechanism, occurring simultaneously at many locations in the interface.

Using the same test, the ZOI was adapted to calculate displacements only on the *Cu* surface, and using the approach detailed in the appendix, the axial strains were calculated from the averaged displacements and are represented in Fig. 13. These strains can be coupled with fatigue

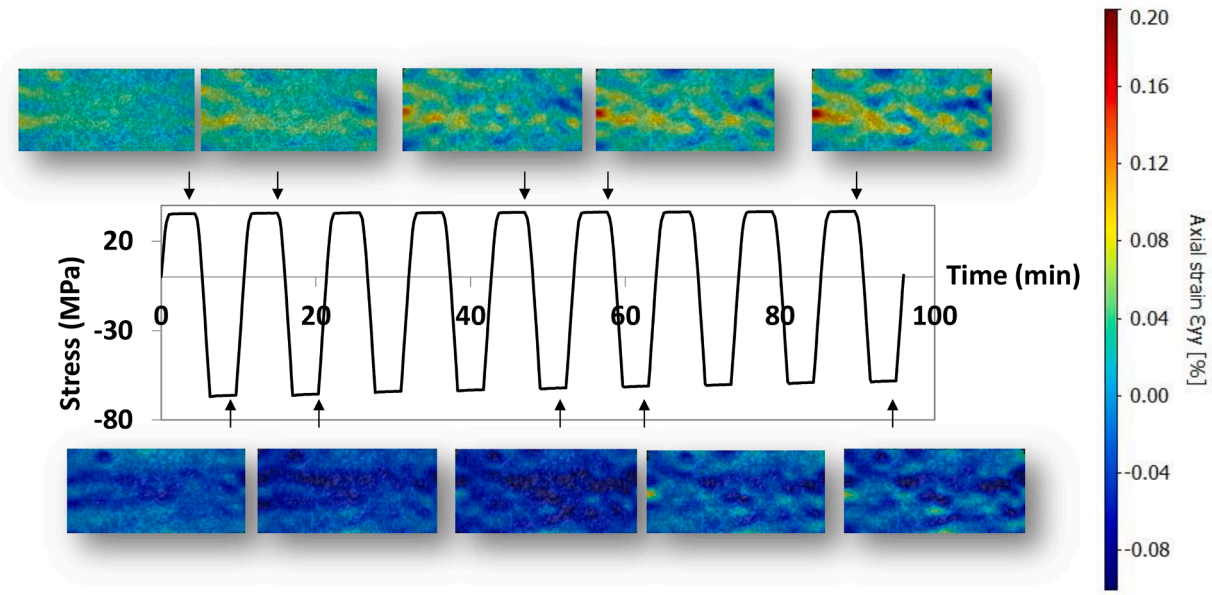

-a-

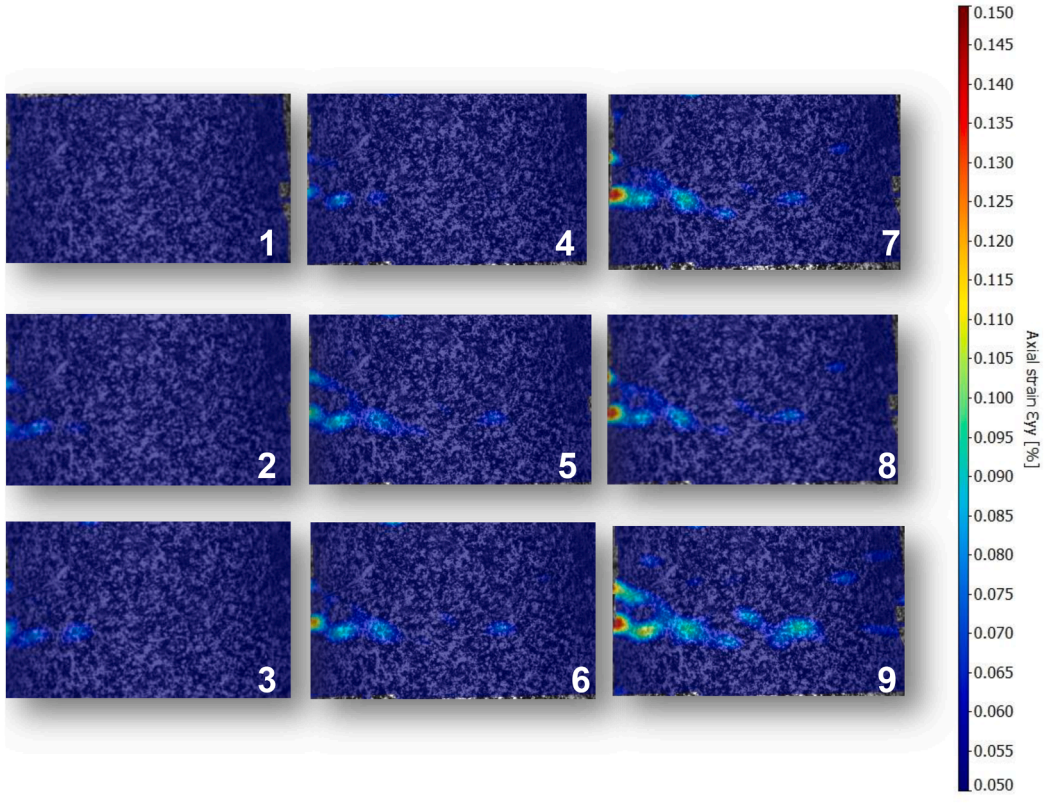

-b-

Fig. 11. Creep-fatigue test with 200 s dwell time coupled with DIC axial strain maps calculated at the end of dwell time (-a-) and at the end of each dwell time in tension for all cycles with an appropriate scale (-b-).

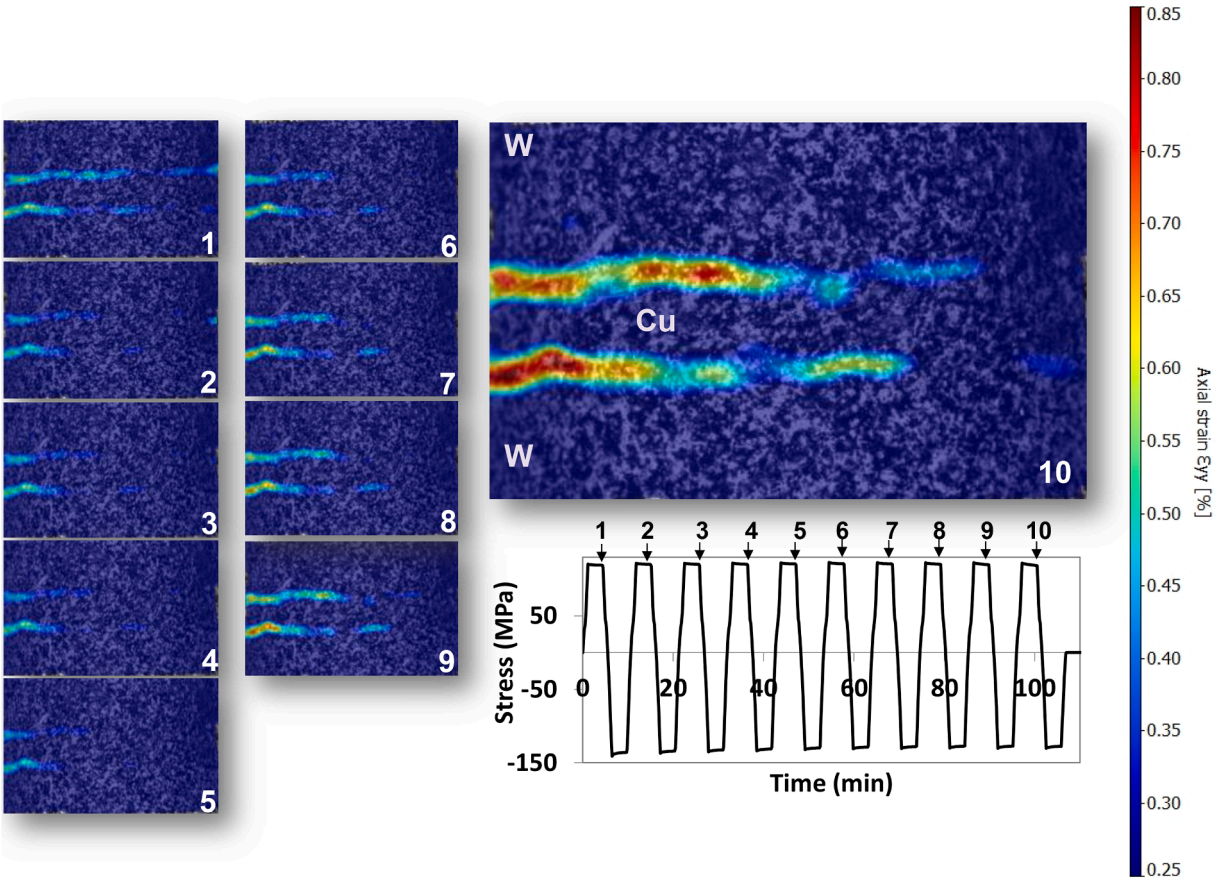

Fig. 12. Axial strain distribution evolution along creep-fatigue test (±1%).

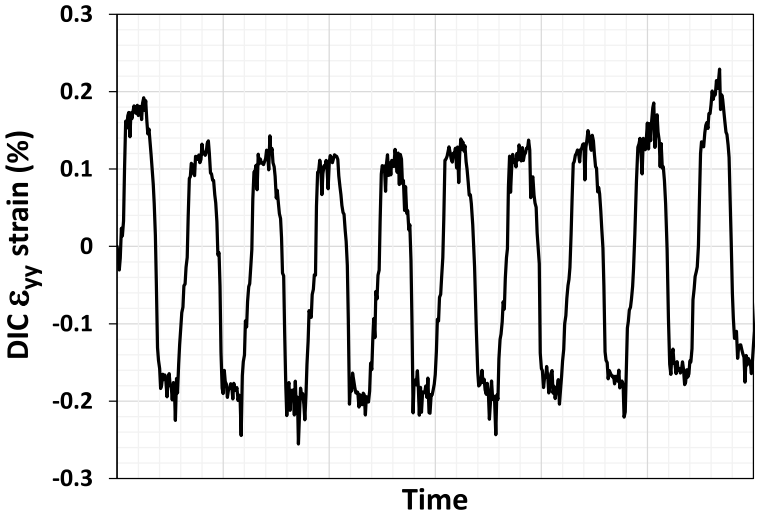

Fig. 13. The evolution of Cu DIC axial strains through the creep-fatigue cycles.

curves for the creep-fatigue life assessment using RCC-MRx or R5 to estimate the allowable creep-fatigue cycles [35]. The standard deviation for DIC strains calculated during the compressive/tensile dwells is ±0.018%.

An additional test was conducted on another sample until the apparition of a visible crack in the recorded DIC images (Fig. 14a). This test confirms the occurrence of material rupture in the interface between *Cu* and *W* (Fig. 14b) as explained above.

As part of our planned future work, we aim to conduct neutron diffraction of the samples to estimate the residual stress and their effect on the deformation of the material. We will complement the experimental residual stress measurement program with Finite Element Analysis (FEA) to replicate the results, considering the difference between the experimental and real geometries. This FEA model will then be applied to the real geometry.

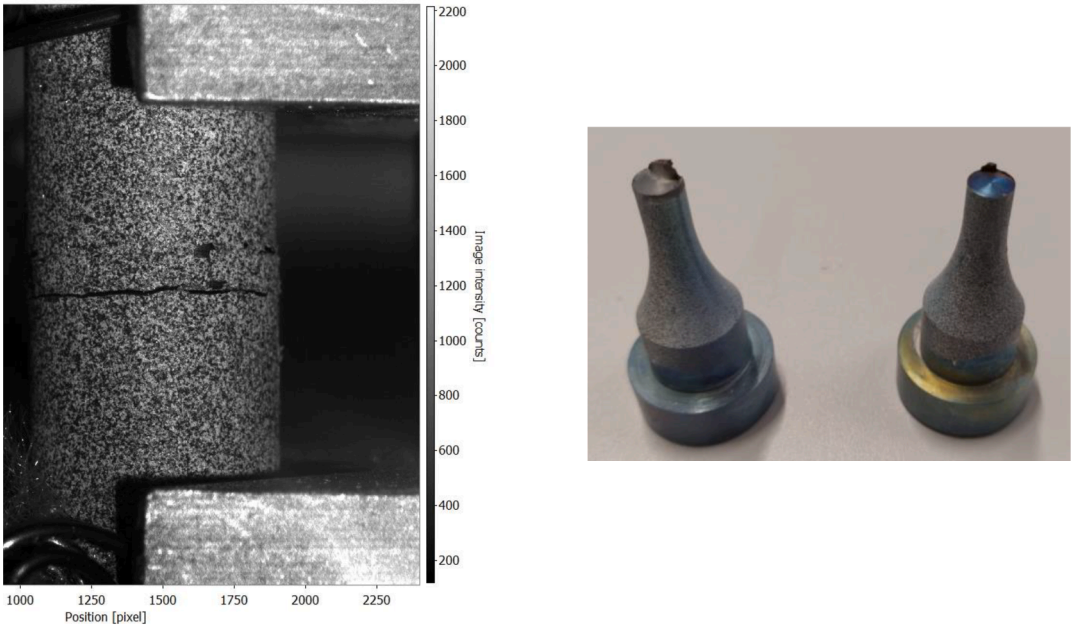

Fig. 14. Material failure after creep-fatigue test occurs on the interface (-b-) confirming the DIC results (-a-).

4. Conclusion

DEMO represents a significant milestone in the progression towards sustainable fusion energy. *W/Cu* material systems are promising candidates to deal with intense thermomechanical loads and irradiation damage expected to be faced by divertor components in this device.

The experimental results presented in this study provide valuable insights into the understanding of the thermomechanical behaviour of *W/Cu* under high-temperature conditions mimicking the expected mono-block conditions in the absence of irradiation.

- Full-field strain measurement using Digital Image Correlation (*DIC*) has been successfully applied to identify interface properties, which can be used directly for design purposes[35] and enabled analysis of local tensile loading experienced in *Cu* brazing due to thermal expansion mismatch even under global compressive loading, leading to tensile creep deformation that must be considered in a life assessment in a divertor component design, where *W* is brazed to a thin layer of *Cu*. To do so, *Cu* is selected as the material to dictate the service life of this weldment as fatigue damage of *W* armor does not accumulate, and the service life of the divertor is determined from the thermal fatigue of either the braze interface region or the copper substrate heat sink [20].
- All signs point to residual tension due to the coefficient of thermal expansion mismatch, which persists in the sample when subjected to global compression and thus leads to progressive creep damage under creep-fatigue loading. These components may experience creep damage at the interface even when global stresses are assumed compressive, which is something not currently considered in RCC-MRx/R5 [35].
- Comparative studies with and without a creep dwell demonstrate accumulation of local creep strain in the *Cu* interface occurs, making creep-fatigue and not thermal fatigue the primary life-limiting mechanism for these components.
- Creep strain accumulated under local tension leads to damage and ultimate failure of the join along the *W/Cu* interface. This has been proven using *DIC* in redundant tests to failure. The absence of sample buckling or shift between brazed surfaces due to compressive loading confirms the structural integrity of the joints at these conditions.

In conclusion, the paper enhances the current knowledge of the thermomechanical behaviour of *W-Cu* joints and contributes to the ongoing efforts in designing efficient and reliable divertor plates for fusion reactors like DEMO.

CRediT authorship contribution statement

Younes Belrhiti: Writing – review & editing, Writing – original draft, Investigation, Formal analysis, Data curation, Visualization. **Cory Hamelin:** Writing – review & editing, Supervision, Funding acquisition, Formal analysis. **David Knowles:** Writing – review & editing, Supervision, Formal analysis. **Mahmoud Mostafavi:** Supervision, Methodology, Funding acquisition.

Declaration of competing interest

Cory Hamelin reports financial support was provided by Engineering and Physical Sciences Research Council. Mahmoud Mostafavi reports financial support was provided by Royal Academy of Engineering. If there are other authors, they declare that they have no known competing financial interests or personal relationships that could have appeared to influence the work reported in this paper.

Data availability

To obtain further information on the data and models underlying this paper please contact PublicationsManager@ukaea.uk

Acknowledgements

This work has been part-funded by the EPSRC Energy Programme, grant number EP/W006839/1, RAEng Fellowship, grant number RCSRF1920\9\46 and EUROfusion programme.

To obtain further information on the data and models underlying this paper please contact PublicationsManager@ukaea.uk*.

The authors would like also to extend their gratitude and special thanks to:

UK Atomic Energy Authority, Culham Science Centre:

Dr Yiqiang Wang for conceptualization
Dr Nicolas Mantel for materials manufacturing
University of Bristol High-Temperature Lab Technical Support Team: Dr Mehdi Mokhtari (Technical Specialist) and Matt Bland (Specialist Technician) for their valuable help

Supplementary materials

Supplementary material associated with this article can be found, in the online version, at doi:10.1016/j.fusengdes.2024.114608.

Appendix: Identification of thermal expansion coefficients using DIC

As thermal expansion coefficients of *W* are not available for all temperatures in the literature, DIC has been used here to estimate the thermal expansion values at different temperatures using the DIC axial strain. To do so, it was necessary to optimize the DIC measurement quality. To this end, a rigid body displacement of 1 mm was applied and then calculated using DIC (Fig. 15a). Different images were recorded, and 50 images were selected. Considering no deformation is assumed to take place in the specimen, it is expected that the assessed displacement is 1 mm everywhere and the strain is zero. DIC axial strain maps of the noise at 400 °C (ε_{yy}) were calculated and the standard deviation was evaluated $\sigma(\mu\varepsilon_{yy})$=86 which indicates the accuracy of the strain measurement for this sample.

For thermal expansion coefficient determination, the displacements computed were exported from StrainMaster software using different smoothing factors (Fig. 15b). The smoothing factor refers to a parameter implemented in LAVISION, serving as a filter to reduce noise in the measured displacements and strains. It is worth mentioning that the electromechanical machine introduces additional errors due to minor movements and oscillations while in a stationary loaded state. Additionally, the glass viewing window can contribute to optical errors. This is why the best practice for noise assessment in DIC according to the iDIC guide [38] is to perform tests with rigid body translation of a sample.

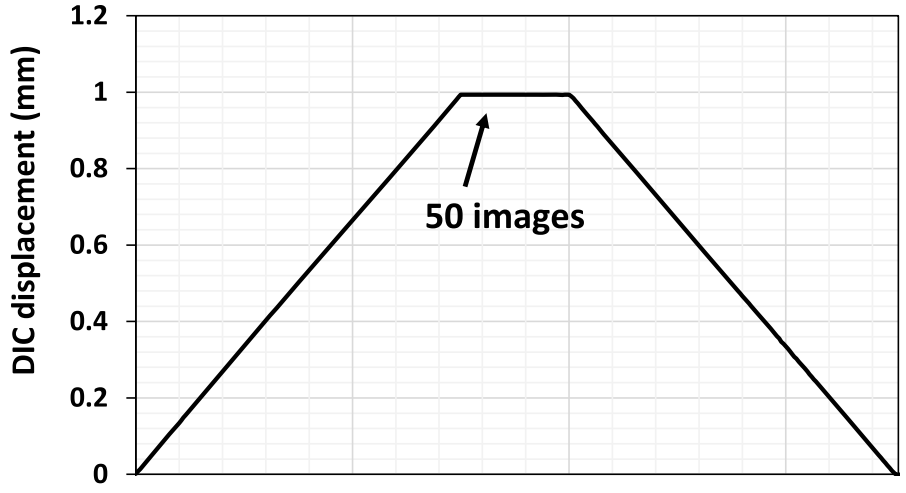

-a-

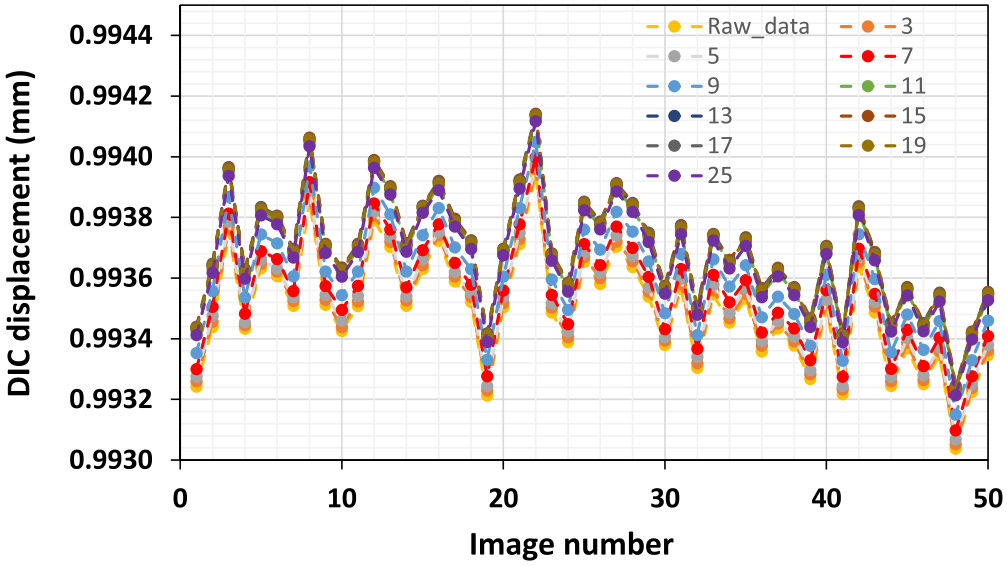

-b-

Fig. 15. DIC displacements exported using different smoothing factors quoted in the legend (-b-) of the 50 images corresponding to an imposed displacement of 1 mm (-a-).

Considering the standard deviation and the difference between the measured displacements and the applied one, smoothing factors 17 and 19 were selected for the following steps. Using the exported displacements from StrainMaster, the normalised thermal expansion is calculated separately and represented in Fig. 16a at the location shown in Fig. 16c corresponding to *W*.

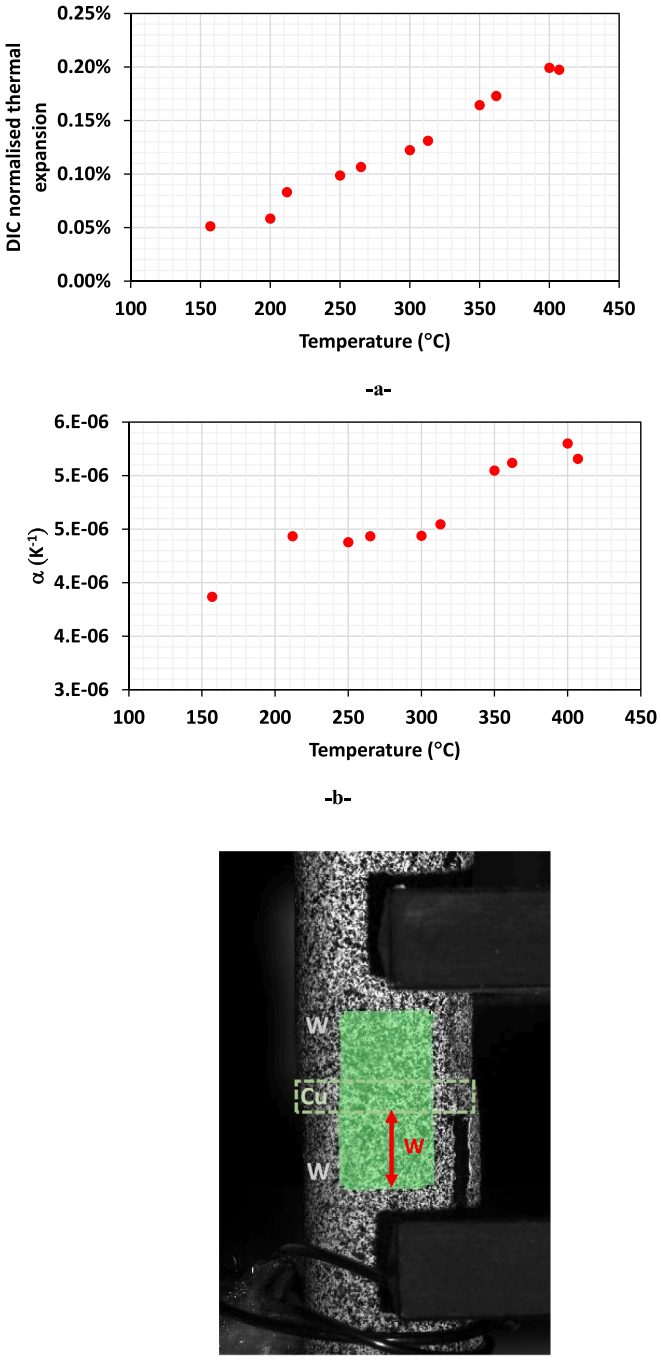

Fig. 16. DIC normalised thermal expansion (-a-) used in the calculation for the thermal expansion coefficient (-b-) of W (-c-).

From these DIC measurements, the thermal expansion coefficient values of *W*, represented in Fig. 16b, are calculated using the following equation:

$$\alpha = \frac{\Delta L}{l_0(\Delta T)} \tag{1}$$

where:

- ΔL is the length variation

- l_0 is the initial length at T_0=25 °C
- $\Delta T = T - T_0$ where T is the analysed temperature

The calculated W values (Fig. 16) using DIC are close to the available values in the literature [9]. Thanks to DIC it was possible to identify additional material properties at high temperatures not yet available in the literature and are not yet included in any materials property handbook as the properties vary significantly depending on suppliers, product forms and even from batch to batch of the same product from the same supplier [3].

References

[1] J.H. You, A review on two previous divertor target concepts for DEMO: mutual impact between structural design requirements and materials performance, Nucl. Fusion 55 (2015) 113026.
[2] P. Frosi, G. Mazzone, J.H. You, Structural design of DEMO Divertor cassette body: provisional FEM analysis and introductive application of RCC-MRx design rules, Fusion Eng. Des. 109–111 (2016) 47–51.
[3] M. Gorley, et al., The EUROfusion materials property handbook for DEMO in-vessel components—status and the challenge to improve confidence level for engineering data, Fusion Eng. Des. 158 (2020) 111668.
[4] M. Gorley, et al., DEMO structural materials qualification and development, Fusion Eng. Des. 170 (2021) 112513.
[5] T. Hirai, et al., Use of tungsten material for the ITER divertor, Nucl. Mater. Energy 9 (2016) 616–622.
[6] M. Li, J.H. You, Structural impact of creep in tungsten monoblock divertor target at 20 MW/m 2, Nucl. Mater. Energy 14 (2018) 1–7.
[7] A.v. Müller, et al., Application of tungsten–copper composite heat sink materials to plasma-facing component mock-ups, Phys. Scr. 2020 (2020) 014015.
[8] K. Yamauchi, N. Sano, K. Tanabe, Direct Tungsten/Copper Bonding for Divertor application, Plasma Fusion Res. 17 (2022), 1405049–1405049.
[9] S. Wang, Y. Wang, Q. Yan, C. Ge, Numerical analysis of fatigue behaviors for tungsten armor of ITER divertor, Nucl. Mater. Energy 25 (2020) 100815.
[10] Y. Zhang, et al., Interfacial metallurgy study of brazed joints between tungsten and fusion related materials for divertor design, J. Nucl. Mater. 454 (2014) 207–216.
[11] Q. Li, et al., Development and application of W/Cu flat-type plasma facing components at ASIPP, Phys. Scr. 2017 (2017) 014020.
[12] M. Tokitani, et al., Potential of copper alloys using a divertor heat sink in the helical reactor FFHR-d1 and their brazing properties with tungsten armor by using the typical candidate filler materials, Plasma Fusion Res. 10 (2015), 3405035–3405035.
[13] M. Tokitani, et al., Advanced multi-step brazing for fabrication of a divertor heat removal component, Nucl. Fusion 61 (2021) 046016.
[14] N. Hara, et al., Mechanical property changes and irradiation hardening due to dissimilar metal welding with reduced activation ferritic/martensitic steel and 316L stainless steel, Fusion Sci. Technol. 56 (2009) 318–322.
[15] H. Fu, et al., Dissimilar-metals bonding between NIFS-HEAT-2 vanadium alloy and Hastelloy X Nickel alloy by controlling intermetallics, Fusion Sci. Technol. 72 (2017) 680–685.
[16] S. Jiang, et al., Interfacial characterization of dissimilar-metals bonding between vanadium alloy and Hastelloy X alloy by explosive welding, J. Nucl. Mater. 539 (2020) 152322.
[17] X. Wu, et al., Bonding strength evaluation of explosive welding joint of tungsten to ferritic steel using ultra-small testing technologies, Mater. Sci. Eng. A 826 (2021) 141995.
[18] K. Yabuuchi, et al., Effects of tool rotation speed on the mechanical properties and microstructure of friction stir welded ODS steel, Mater. Sci. Eng. A 595 (2014) 291–296.
[19] H. Serizawa, et al., Influence of friction stir welding conditions on joinability of V-alloy/SUS316L dissimilar joint, Nucl. Mater. Energy 15 (2018) 43–47.
[20] T. Horie, M. Seki, A. Minato, T. Tone, Analysis and experiments on lifetime predictions for first wall and Divertor plate structures in JAERI, Fusion Technol. 10 (1986) 753–758.
[21] M. Dias, et al., New WC-Cu composites for the divertor in fusion reactors, J. Nucl. Mater. 521 (2019) 31–37.
[22] M. Mostafavi, T.J. Marrow, Quantitative in situ study of short crack propagation in polygranular graphite by digital image correlation, Fatigue Fract. Eng. Mat. Struct. 35 (2012) 695–707.
[23] Y. Belrhiti, et al., Application of optical methods to investigate the non-linear asymmetric behavior of ceramics exhibiting large strain to rupture by four-points bending test, J. Eur. Ceram. Soc. 32 (2012) 4073–4081.
[24] Belrhiti, Y. Strain fields measurements to study the nonlinear mechanical behaviour of refractory materials. (Limoges, 2015).
[25] Y. Belrhiti, et al., Investigation of the impact of micro-cracks on fracture behavior of magnesia products using wedge splitting test and digital image correlation, J. Eur. Ceram. Soc. 35 (2015) 823–829.
[26] Y. Belrhiti, et al., Combination of Brazilian test and digital image correlation for mechanical characterization of refractory materials, J. Eur. Ceram. Soc. 37 (2017) 2285–2293.
[27] S.M. Barhli, M. Mostafavi, A.F. Cinar, D. Hollis, T.J. Marrow, J-Integral calculation by finite element processing of measured full-field surface displacements, Exp. Mech. 57 (2017) 997–1009.
[28] A.F. Cinar, et al., An autonomous surface discontinuity detection and quantification method by digital image correlation and phase congruency, Opt. Lasers Eng. 96 (2017) 94–106.
[29] R. Jiang, et al., Strain accumulation and fatigue crack initiation at pores and carbides in a SX superalloy at room temperature, Int. J. Fatigue 114 (2018) 22–33.
[30] A. Harte, et al., Deformation heterogeneity in laser-welded Eurofer, Fusion Eng. Des. 161 (2020) 111860.
[31] A. Harte, et al., Deformation heterogeneity in laser-welded Eurofer, Fusion Eng. Des. 161 (2020).
[32] V.D. Vijayanand, et al., A novel methodology for estimating tensile properties in a small punch test employing in-situ DIC based deflection mapping, J. Nucl. Mater. 538 (2020).
[33] M. van Rooyen, T. Becker, M. Mostafavi, An experimental approach to the application of digital image correlation to small punch creep testing, in: Proceedings of the MATEC Web of Conferences 34700026, EDP Sciences, 2021.
[34] Y. Zhao, R. Jiang, A. Harte, D.J. Bull, P.A.S Reed, Characterisation of strain localisation under cyclic loading at 450°C by SEM-DIC in a PM Ni-based superalloy, Mater. Sci. Eng. A 849 (2022).
[35] Y. Belrhiti, C. Hamelin, D. Knowles, M. Mostafavi, Life assessment of metals used in fusion using R5 and RCC-MRx, in: Proceedings of the ASME 2024 Pressure Vessels & Piping Conference PVP2024-122776, 2024.
[36] You, J.H., Mantel, N. & Fursdon, M. Further development of the IAP for creep and application of IAP to cassette. DIV-2.9.4-T004-D001.
[37] Z. Pan, S. Huang, Y. Su, M. Qiao, Q. Zhang, Strain field measurements over 3000°C using 3D-digital image correlation, Opt. Lasers Eng. 127 (2020) 105942.
[38] International Digital Image Correlation Society, A Good Practices Guide for Digital Image Correlation, International Digital Image Correlation Society, 2018 (eds. Jones, E. & Iadicola, M.).
[39] LaVision GmbH, L. StrainMaster. 2024.
[40] M. Li, S.J. Zinkle, Physical and mechanical properties of copper and copper alloys, Compr. Nucl. Mater. (2012) 667–690.